J|A|C|S ARTICLES

Published on Web 12/23/2008

Investigation of the Internal Heterostructure of Highly Luminescent Quantum Dot−Quantum Well Nanocrystals

Pralay K. Santra,[†] Ranjani Viswanatha,[†] Steve M. Daniels,[‡] Nigel L. Pickett,[§] Jason M. Smith,[||] Paul O'Brien,[‡] and D. D. Sarma*[,†,⊥,#]

Solid State and Structural Chemistry Unit, Indian Institute of Science, Bangalore 560012, India, Department of Chemistry, University of Manchester, Manchester M13 9PL, U.K., Nanoco Technologies Ltd., 46 Grafton Street, Manchester M13 9XX, U.K., Department of Materials, University of Oxford, Oxford OX1 3PH, U.K., and Centre for Advanced Materials, Indian Association for the Cultivation of Science, Kolkata 700032, India

Received May 4, 2008; Revised Manuscript Received November 17, 2008; E-mail: mlsdds@iacs.res.in

Abstract: In this paper, we report on the growth and characterization of quantum dot−quantum well nanostructures with photoluminescence (PL) that is tunable over the visible range. The material exhibits a PL efficiency as high as ∼60% and is prepared by reacting ZnS nanocrystals in turn with precursors for CdSe and ZnS in an attempt to form a simple "ZnS/CdSe/ZnS quantum-well structure". Through the use of synchrotron radiation-based photoelectron spectroscopy in conjunction with detailed overall compositional analysis and correlation with the size of the final composite nanostructure, the internal structure of the composite nanocrystals is shown to consist of a graded alloy core whose composition gradually changes from ZnS at the very center to CdSe at the onset of a CdSe layer. The outer shell is ZnS with a sharp interface, probably reflecting the relative thermodynamic stabilities of the parent binary phases. These contrasting aspects of the internal structure are discussed in terms of the various reactivities and are shown to be crucial for understanding the optical properties of such complex heterostructured nanomaterials.

1. Introduction

In recent years, there has been considerable interest in semiconductor nanoparticles with diverse internal heterostructures, mainly because of their potential applications in various fields, such as telecommunications,[1] light-emitting diodes and displays,[2] optoelectronics,[3] biosensing and biolabeling,[4−8] and quantum-dot lasers.[9] Several methods have been established for the synthesis of such heterostructured semiconductor nanoparticles, and a large percentage of them show interesting tunable optical properties due to quantum confinement effects. An interesting variant on the basic theme is the so-called "quantum dot−quantum well" (QDQW),[10−16] which is synthesized with a core of a large-band-gap material followed by two shells, the inner one consisting of a small-band-gap material and the outer one of the same large-band-gap material as the core. These structures are immediately attractive since they allow independent control of the band gap and nanocrystal size. In general, such heterostructures have been implicitly assumed to have sharp interfaces between the constituent layers without significant intermixing/alloying. Such atomically sharp and pure interfaces are routinely produced in thin films (e.g., in the growth of semiconductor devices by molecular beam epitaxy), and the quality of these planar interfaces can be verified accurately using cross-sectional electron microscopy. However, the situation is considerably more complex in the case of these *nano*materials. The chemical process used for synthesizing such heterostructures may facilitate intermixing of the phases by ion exchange between the nanocrystal constituents and the reactants in the chemical bath. Ostwald and other ripening processes may play

[†] Indian Institute of Science.
[‡] University of Manchester.
[§] Nanoco Technologies Ltd.
[||] University of Oxford.
[⊥] Indian Association for the Cultivation of Science.
[#] Also at Jawaharlal Nehru Centre for Advanced Scientific Research, Bangalore 560054, India.

(1) Ramdane, A.; Ougazzaden, A. *Mater. Sci. Eng., B* **2000**, *74*, 66.
(2) Coe, S.; Woo, W.-K.; Bawendi, M.; Bulovic, V. *Nature* **2002**, *420*, 800.
(3) Murphy, C. J. *Anal. Chem.* **2002**, *74*, 520.
(4) Bruchez, M., Jr.; Moronne, M.; Gin, P.; Weiss, S.; Alivisatos, A. P. *Science* **1998**, *281*, 2013.
(5) Akerman, M. E.; Chan, W. C. W.; Laakkonen, P.; Bhatia, S. N.; Ruoslahti, E. *Proc. Natl. Acad. Sci. U.S.A.* **2002**, *99*, 12617.
(6) Dubertret, B.; Skourides, P.; Norris, D. J.; Noireaux, V.; Brivanlou, A. H.; Libchaber, A. *Science* **2002**, *298*, 1759.
(7) Wu, X.; Liu, H.; Liu, J.; Haley, K. N.; Treadway, J. A.; Larson, J. P.; Ge, N.; Peale, F.; Bruchez, M. P. *Nat. Biotechnol.* **2003**, *21*, 41.
(8) Jaiswal, J. K.; Mattoussi, H.; Mauro, J. M.; Simon, S. M. *Nat. Biotechnol.* **2003**, *21*, 47.
(9) Chan, W. C. W.; Nie, S. *Science* **1998**, *281*, 2016.
(10) Mews, A.; Eychmüller, A.; Giersig, M.; Schooss, D.; Weller, H. *J. Phys. Chem.* **1994**, *98*, 934.
(11) Schooss, D.; Mews, A.; Eychmüller, A.; Weller, H. *Phys. Rev. B* **1994**, *49*, 17072.
(12) Mews, A.; Kadavanich, A. V.; Banin, U.; Alivisatos, A. P. *Phys. Rev. B* **1996**, *53*, 13242.
(13) Lifshitz, E.; Porteanu, H.; Glozman, A.; Weller, H.; Pflughoefft, M.; Eychmüller, A. *J. Phys. Chem.* **1999**, *103*, 6870.
(14) Braun, M.; Burda, C.; Mohamed, M.; El-Sayed, M. *Phys. Rev. B* **2001**, *64*, 035317.
(15) Bryant, G. W.; Jaskólski, W. *Phys. Rev. B* **2003**, *67*, 205320.
(16) Berezovsky, J.; Ouyang, M.; Meier, F.; Awschalom, D. D.; Battaglia, D.; Peng, X. *Phys. Rev. B* **2005**, *71*, 081309.

10.1021/ja8033075 CCC: $40.75

important roles in the chemical syntheses of nanomaterials[17,18] and serve to demonstrate the importance of ion exchange between the nanoparticles and the solution, even for a simpler core-only structure. Moreover, there has been no generally applicable experimental technique capable of establishing the nature or existence of the interfaces within heterostructured nanocrystals. Cross-sectional analysis is not possible because of the small size of the particles, and in high-resolution transmission electron microscopy (HRTEM), most material combinations reveal insufficient contrast between different layers as a result of the small layer thicknesses and the existence of the surface and associated defects/disorders.[19] It has proved difficult, if not impossible, to understand the nature of the heterostructures in general and the interfaces in particular for all but a few exceptional examples.[20] The lack of characterization has been a serious hindrance in developing heterostructures, since any deviation from the assumed ideal interface/structure is likely to have a significant influence on the electronic and optical properties of such nanostructures.

Other than TEM, as discussed above, no single technique has yet demonstrated an ability to determine the compositional variation inside a heterostructured nanoparticle. In this context, we recall that X-ray photoelectron spectroscopy (XPS) has been often used to determine the composition of bulk materials as well as surfaces and is often called "electron spectroscopy for chemical analysis" (or ESCA). In a twist to this capability of determining the composition, Nanda et al.[21,22] first used XPS successfully to determine the internal structure and total size of homogeneous CdS and ZnS spherical nanoparticles capped with 1-thioglycerol, a technique that was later shown to be applicable to nonspherical nanoparticles.[23] The same technique was also applied to probe heterostructured QDQWs.[24] However, the possibility of any alloy formation between the different shells could not be addressed in such studies; moreover, the individual thicknesses of the different outer shells could not be determined with any confidence. Therefore, the development of reliable and widely applicable techniques for probing the internal composition of heterostructured nanocrystals remains an outstanding challenge.

In this work, we have studied ZnS/CdSe/ZnS/capping agent QDQW structures, and we will show that by combining XPS (using different photon energies with the high flux available at a third-generation synchrotron source) with average chemical composition analysis and TEM-image particle sizing, we can *unambiguously* determine the internal structure of such complicated nanomaterial systems. Also, we will show how this detailed knowledge of the internal structure of QDQWs leads to a consistent and remarkably accurate description of their optical properties.

2. Experimental Section

Triethylamine (Sigma Aldrich, 99%), benzenethiol (Sigma Aldrich, 98%), zinc nitrate hexahydrate (Sigma Aldrich, 98%), cadmium nitrate tetrahydrate (Sigma Aldrich, 99%), sulfur powder (Sigma Aldrich, reagent grade, ~100 mesh), selenium powder (Sigma Aldrich, 99.99%, ~100 mesh), hexadecylamine (Alfa Aesar, tech grade, 90%), hexamethyldisilathiane (Sigma Aldrich, reagent grade, 97%), trioctylphosphine (Sigma Aldrich, tech grade, 90%), and diethylzinc (Strem Chemicals, min 95%) were used in the preparations described here. All of the solvents used were of analytical grade and purchased from Fisher. All of the chemicals and solvents were used without further purification.

A 0.38 g sample of the Zn/S single precursor, $[Et_3NH]_4[Zn_{10}S_4(SPh)_{16}]$, which was prepared using a method reported previously,[25] was added to a flask containing 20 g of degassed hexadecylamine at 100 °C under an argon flow. The solution was heated to 300 °C for 30 min to form ZnS cores and then cooled to 60 °C. From this solution, the product was isolated using methanol until flocculation was observed. The flocculated particles were centrifuged, and the supernatant was discarded. A small volume of toluene was added to the wet pellet to completely disperse the solid sample. The procedure was repeated two more times to completely remove any trace of unreacted starting materials. The UV absorption and photoluminescence (PL) spectra along with a TEM image of these purified cores are shown in Figure S1 in the Supporting Information. Typically, 35 mg of these purified ZnS cores was transferred to a flask containing 10 g of fresh degassed hexadecylamine at 100 °C. The degassed single precursor for Cd and Se, $[Et_3NH]_4[Cd_{10}Se_4(SPh)_{16}]$, was added slowly in small amounts of ~2.5 mg at 150 °C over a period of 2 min under an Ar flow, and the UV−vis absorption and PL emission spectra were continuously monitored. The UV−vis and PL peaks progressively shifted to longer wavelengths with increasing addition of the Cd/Se precursor, and addition of this precursor was stopped when the required emission wavelength was obtained. While the amount of Cd/Se precursor added to the reaction mixture was determined by monitoring the shift in the emission wavelength, the absence of any separate PL peak arising from homogenously nucleated CdSe nanoparticles in our results suggests that most of the Cd/Se precursor added to the reaction mixture was consumed in overcoating the ZnS cores, as long as the precursor was added slowly. In particular, we did not observe any PL signal that could be attributed to such homonucleated CdSe nanoparticles even after the final step of passivating the nanoparticles with the outermost ZnS layer. Additionally, we did not see any small-sized nanoparticles in TEM images either. However, in control experiments, when the Cd/Se precursor was added too fast (e.g., the whole amount in one step), formation of homogenously nucleated CdSe was observed. To prepare[26,27] the final ZnS layer, the ZnS/CdSe core−shells were added to 10 g of freshly degassed hexadecylamine and heated to 180 °C, after which the ZnS shell was grown by alternate dropwise additions of 0.1 M solutions of diethylzinc and hexamethyldisilathiane in trioctylphosphine until the maximum PL intensity was observed, typically at ~1 monolayer thickness, by monitoring with an in situ PL intensity probe. Finally, the reaction mixture was cooled to 60 °C, and ZnS/CdSe/ZnS QDQWs were isolated with methanol.

The shape and crystallinity of the synthesized QDQWs were characterized by TEM and X-ray diffraction (XRD). The TEM measurements were performed using a Technai F30 UHR electron microscope operating at an accelerating voltage of 300 kV. The samples for TEM were prepared by dispersing the diluted QDQW samples in hexane on carbon-coated Cu grids. The chemical

(17) Viswanatha, R.; Santra, P. K.; Dasgupta, C.; Sarma, D. D. *Phys. Rev. Lett.* **2007**, *98*, 255501.
(18) Viswanatha, R.; Amenitsch, H.; Sarma, D. D. *J. Am. Chem. Soc.* **2007**, *129*, 4470.
(19) Alivisatos, A. P. *J. Phys. Chem.* **1996**, *100*, 13226.
(20) Liz-Marzan, L. M.; Giersig, M.; Mulvaney, P. *Langmuir* **1996**, *12*, 4329.
(21) Nanda, J.; Kuruvilla, B. A.; Sarma, D. D. *Phys. Rev. B* **1999**, *59*, 7473.
(22) Nanda, J.; Sarma, D. D. *J. Appl. Phys.* **2001**, *90*, 2504.
(23) Sapra, S.; Nanda, J.; Pietryga, J. M.; Hollingsworth, J. A.; Sarma, D. D. *J. Phys. Chem. B* **2006**, *110*, 15244.
(24) Borchert, H.; Dorfs, D.; McGinley, C.; Adam, S.; Möller, T.; Weller, H.; Eychmüller, A. *J. Phys. Chem. B* **2003**, *107*, 7486.
(25) Dance, I. G.; Choy, A.; Scudder, M. L. *J. Am. Chem. Soc.* **1984**, *106*, 2682.
(26) Daniel, S. M. Ph.D. Thesis, University of Manchester, Manchester, U.K., 2006.
(27) Pickett, N.; Daniel, S. M.; O'Brien, P. U.K. Patent GB2429838A, 2007.

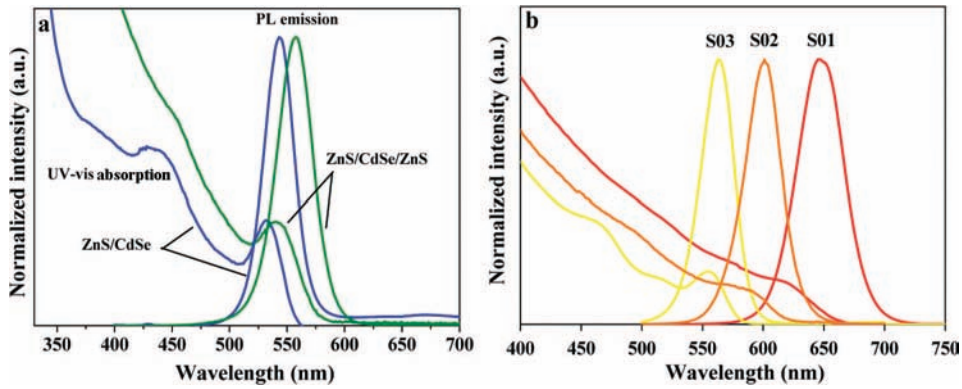

Figure 1. (a) UV−vis absorption and PL spectra of ZnS/CdSe (blue) and ZnS/CdSe/ZnS (green). (b) Absorption and band-edge emission spectra of the three samples S01 (red), S02 (orange), and S03 (yellow) whose internal heterostructures were determined by X-ray photoemission spectroscopy.

composition of the QDQWs was measured by inductively coupled plasma−atomic emission spectroscopy (ICP−AES) using a PerkinElmer Optima 2100 DV spectrometer. The in situ PL spectra were monitored by inserting into the solution one end of an optical fiber (from an Ocean Optics USB 2000) that was connected to the detector at the other end. The nanocrystals were excited by shining a UV lamp from the outside.

To perform the photoemission experiments on these QDQWs, the dried samples were thoroughly mixed with graphite to avoid charging during the photoemission process. The mixture of the sample and graphite was stuck to the sample holder using conducting Ag paste. The X-ray photoemission experiments at lower photon energies (750 and 615 eV) were performed at the vacuum ultraviolet (VUV) beamline (operating at 2 GeV ring energy) at ELETTRA, the Italian synchrotron center in Trieste. Experiments using higher energies (1486.6 and 1253.6 eV) were performed using a commercially available X-ray photoemission spectrometer from VSW Scientific Instruments. To ensure the absence of any synchrotron radiation-induced damage of the samples, we performed experiments at several spots for different time durations and confirmed that the spectra were identical at all of these spots. The C 2s signal from graphite was used as the internal reference for the binding energies.

A least-squares fitting procedure[21−23,28] was used to decompose the individual components from distinct species contributing to the XPS signal. Characteristic lifetime broadening for each species contributing to the photoemission signal was simulated using a Lorentzian function, which was then convoluted with a Gaussian function to simulate the instrumental broadening. All *n*p and *n*d core-level photoemission signals are known to be split into a doublet structure as a result of spin−orbit interactions. The energy separation between the spin−orbit split doublet signals and their intensity ratio for a given core level are expected to remain the same in different compounds, since they are determined by deep atomic core levels with little influence from the environment. Therefore, these quantities were constrained to be identical for a given species in all of our analyses, independent of the sample and the photon energy. Similarly, the lifetime broadening of a given core level does not depend on the photon energy, and therefore, the width of the Lorentzian function for every given core signal was kept fixed in the analysis. On the other hand, the width of the Gaussian function representing the instrumental resolution was constrained to be identical for all of the spectra recorded at a given photon energy.

3. Results and Discussion

The tuning of the emission, spanning most of the visible spectrum from 450 to 650 nm, was achieved for CdSe-capped ZnS (ZnS/CdSe) core−shell structure simply by increasing the amount of Cd/Se precursors in the reaction mixture, as already explained. These core−shell nanocrystals were characterized by UV absorption and PL emission spectroscopy and TEM (Figure S2a,b in the Supporting Information). The quantum-well structure was completed by the addition of an outer shell composed of ZnS. The PL emission was monitored in real time using an in situ probe, which allowed us to increase the shell thickness until the emission intensity peaked at maximum. Figure 1a shows the UV−vis absorption and PL spectra of a ZnS/CdSe core−shell emitting at 543 nm and the corresponding completed QDQW. The QDQW shows a PL red shift of 13 nm due to partial exciton leakage into the outer ZnS shell material.[29] In this manner, which can be scaled to yield multigram quantities, we can easily and reproducibly prepare highly efficient, narrowly dispersed QDQWs that have a narrow emission width, with the PL efficiency reaching 60% for samples with a thin CdSe shell and emitting in the blue. The addition of thicker CdSe layers may create defects due to the larger lattice mismatch between ZnS and CdSe, resulting in nonradiative recombination processes that lower the quantum yield (QY). This is reflected in the red-emitting samples, which had typical QYs of ∼20%. We synthesized three ZnS/CdSe/ZnS QDQW structures by starting with identical inner cores, varying the thickness of the active well layer, and finally adding outer shells to yield the optimum PL intensities of three samples, which are labeled as S01 (red-emitting), S02 (orange-emitting) and S03 (yellow-emitting). The UV−vis absorption and PL spectra of these samples are shown in Figure 1b.

In this report, we will show detailed experimental results only for sample S01, while the data for the other two samples can be found in the Supporting Information. Figure 2a shows a typical TEM image of S01. Analyzing a total of ∼150 nanoparticles, we found that the average radius of the particles was 36.8 Å with a narrow size distribution of 4.8%. The average total radii (r_3) of the three samples obtained from TEM are given in parentheses in Table 1. An HRTEM image of S01 that exhibits lattice fringes is shown in Figure 2b. We were unable to find any internal heterogeneity in these nanoparticles even from a close inspection of the HRTEM images. We selected one of the nanoparticles in the HRTEM image and drew a line along one lattice plane (Figure 2c); the measured intensity profile along that line is shown in Figure 2d. From these analyses, it

(28) Krishnakumar, S. R.; Sarma, D. D. *Phys. Rev. B* **2003**, *68*, 155110.

(29) Dabbousi, B. O.; Rodriguez-Viejo, J.; Mikulec, F. V.; Heine, J. R.; Mattoussi, H.; Ober, R.; Jensen, K. F.; Bawendi, M. G. *J. Phys. Chem. B* **1997**, *101*, 9463.

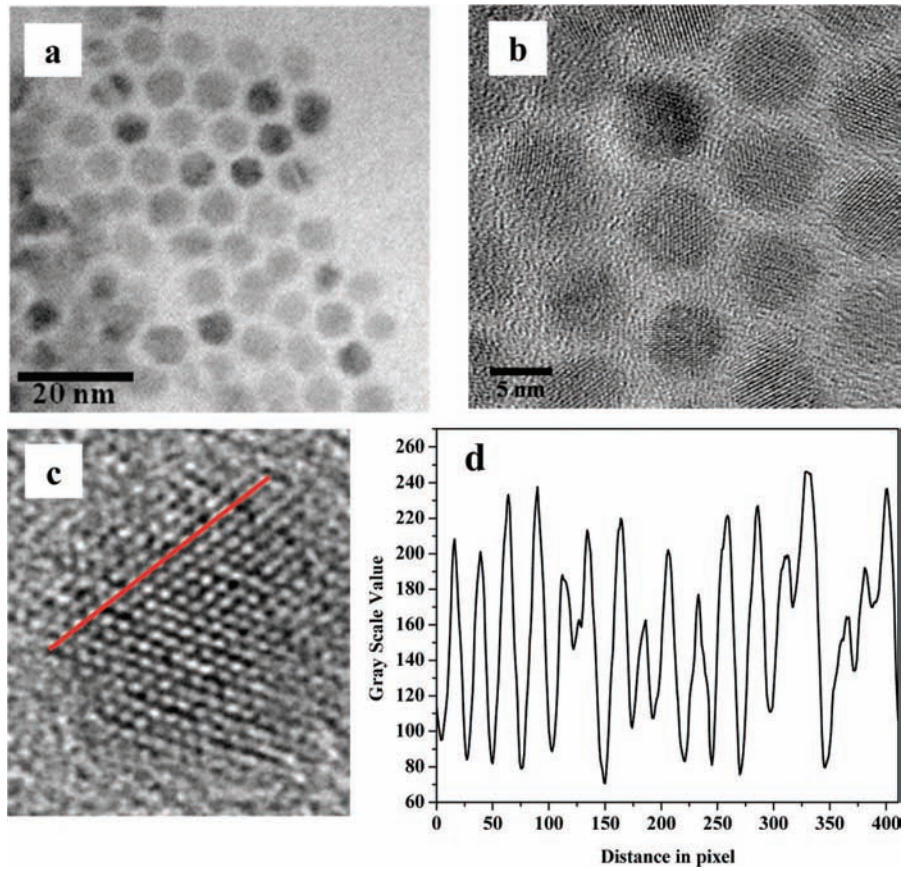

Figure 2. (a) TEM image of the nanoparticles of ZnS/CdSe/ZnS/capping agent. (b) HRTEM image of the same particles. (c) Zoomed HRTEM image of one of the nanoparticles. (d) Line scan along the red line drawn in (c), indicating that HRTEM is unable to determine any inhomogeneity inside the nanoparticles.

Table 1. Values of Various Radii r_1, r_2, and r_3 Defining the QDQW Structure and the Cd/Zn Content Ratio Derived from the Analysis of the Photoemission Data for the Three Samples (r_3 Values Determined from TEM and Cd/Zn Ratios Obtained from ICP−AES Are Shown in Parentheses for Easy Comparison)

sample number	r_1 (Å)	r_2 (Å)	r_3 (Å)	Cd/Zn ratio
S01	19.3	32.2	35.5 (36.8)	1.75 (1.65)
S02	11.5	21.5	25.5 (26.2)	1.08 (1.04)
S03	12.5	19.3	23.1 (21.4)	1.06 (0.99)

was impossible to determine any clear interface separating the various layers within the nanoparticles. This can be due to various reasons, such as the lack of a strong contrast variation across such interfaces, similar crystal structures, and/or intermixing across the interface, leading to a smooth variation of composition and lattice parameters; the last possibility (intermixing), at the extreme end, gives rise to a homogeneous alloy with the same average composition in all parts of the nanoparticle. The XRD pattern of these nanocrystals (shown in Figure S3 in the Supporting Information) establishes that the particles predominantly have the wurtzite structure. We carried out a composition analysis of the samples using ICP−AES, which provided the relative amounts of Cd, Zn, and Se. Accurate estimation of S was not possible with this technique because S reacts with the dilute acid, HCl, giving out H_2S while the samples were dissolving. However, explicit verification carried out for standard dilute acid solutions of Se showed that the concentration of Se did not show any deviation from the estimated values, indicating the absence of formation of H_2Se gas unlike the S counterpart. The ICP−AES-determined Cd/Zn composition ratios for the different samples are given in parentheses in Table 1.

In order to provide the quantitative description of the internal structure of the QDQW particles, we assume the particles to have spherical symmetry, as suggested by the TEM images (Figure 2 and Figure S4 in the Supporting Information), while noting that a generalization to a more anisotropic shape, if needed, is indeed possible.[23] Since the nanoparticles are synthesized by first forming a spherical core of ZnS and then capping successively with layers of CdSe and ZnS, the ideal distributions for the chemical components (e.g., S and Se) in the formed particles, assuming a sharp interface, are as shown in Figure 3a. However, it is plausible that ion exchange involving S and Se ions in consecutive layers does take place, leading to an interface that is diffuse. We illustrate two other possible compositional variations in Figure 3b,c. Figure 3b illustrates a situation where sharp interfaces exist as in Figure 3a, but they are not directly between ZnS and CdSe; instead, a homogeneous alloy phase exists between the pure phases as a result of intermixing at the interface. In contrast, Figure 3c represents a case where the interface is not sharp; the pure phases are connected by a graded interface region across which the composition changes continuously. Clearly, these figures illustrate only some of the possibilities and are to be viewed only as limiting models to provide an approximate description of the reality. We show below that our approach of combining XPS, TEM, and ICP−AES is able to discriminate among these models and allows us to pick out the most suitable description for the QDQWs we have studied, with a quantitative description

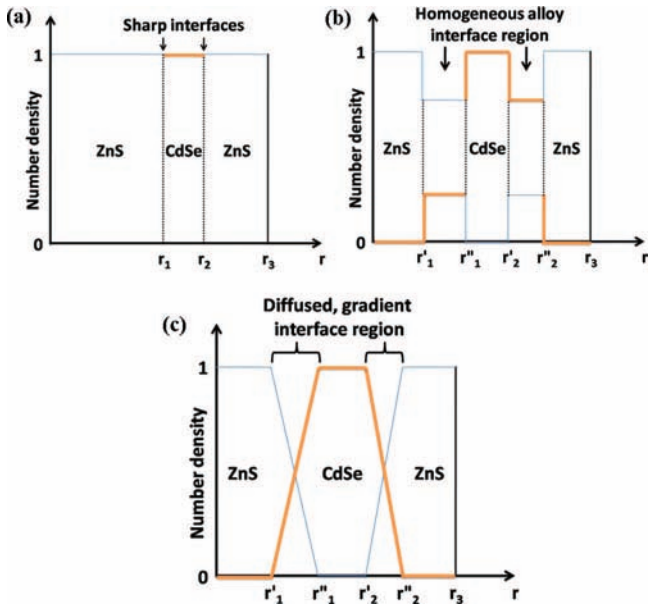

Figure 3. Schematic diagram of different interfaces possible inside a heterostructured nanoparticle. The S number density is shown by the thin blue line and the Se number density by the thick saffron line. The vertical dotted lines show the boundaries between different phases: (a) sharp interfaces are present between the pure phases; (b) homogeneous alloy phases exist between the pure phases, (c) the pure phases are connected by composition-graded regions across which the composition changes continuously.

of all of the parameters characterizing the model. We make critical use of the extreme surface sensitivity of XPS and the rapid tunability of this surface sensitivity by varying the photon energy. These ideas have been illustrated in Figures S5 and S6 in the Supporting Information and discussed in some detail in the text associated with those figures.

There have been several previous efforts[21,22,24,28,30−35] to distinguish the surface composition from that of the bulk using electron spectroscopy data from bulk and nanosized materials. Before we present our XPS data, we would like to stress the unique aspects of the present study compared with all of the previous studies of nanocrystals. The original work[21] from our laboratory used only fixed photon sources (Al Kα and Mg Kα), thereby limiting the surface sensitivity. Kulkarni et al.[33] used a tunable synchrotron source to tune the photon energy and therefore the surface sensitivity of the recorded spectra; however, this study did not attempt any quantitative analysis. Following the quantitative approach in refs 21 and 33, Borchert et al.[34] attempted to quantify the thickness of the overlayer for ZnS-passivated InP nanoparticles. However, several a priori assumptions were made in order to render the analysis tractable. For example, the interface between InP and ZnS was assumed to be sharp, without any intermixing, in obvious contrast to the primary concern in our present work. Additionally, ref 34 also fixed the size of the InP core region to the value measured by TEM for bare InP nanoparticles that were subsequently overcoated with ZnS; this assumption precludes any possibility of a change in the size of the core region due to incorporation of ions from the reaction mixture during the chemical process meant for growing the ZnS overlayer. In a separate work,[24] photoemission studies of QDQWs of CdS and HgS were not successful in determining the nature of the heterostructure or the thicknesses of the outer two shells with confidence. Our approach differs from the previous ones in some important aspects besides the unique combination of ICP−AES and TEM results with analysis of electron spectroscopy data. We choose to analyze the spectral region with overlapping S 2p and Se 3p core-level spectra. While good signal-to-noise ratio in each case allows us reliable spectral decomposition in terms of individual contributions from S 2p and Se 3p separately (as shown later), this method has significant advantages over other methods employed earlier. For example, the appearance of both S 2p and Se 3p signals in the same energy region with the same photon energy allows us to analyze the ratio of the two intensities, thereby ensuring that our results are insensitive to the intensity of the photon source; had we used two different photon energies for two different core-level spectra,[24,34,35] the quantitative analysis would require an additional parameter in the form of the ratio of the photon fluxes at those two energies, which is a difficult quantity to estimate reliably. Additionally, if we choose core-level spectra that appear far apart on the energy scale, we would require two separate mean free paths, one for each core level, for the analysis; with our method, the core-level intensities of the S 2p and Se 3p spectral regions can be characterized by a single mean free path, λ, for both core levels, thereby reducing yet another difficult-to-estimate parameter from our analysis. There have been attempts[36,37] to estimate the value of λ in a material-specific manner. In our analysis also, we obtain the mean free path, λ, for both ZnS and CdSe using the TPP-2 formula.[37] In the kinetic energy interval of our interest, we found that the two materials ZnS and CdSe have almost the same mean free path, within an accuracy of 1.3%, so to a good approximation, the same value of λ can be used for all regions, independent of the form of the heterostructure or the composition of alloys inside the nanoparticle.

The high-resolution core−level spectra of S 2p and Se 3p were taken at three different photon energies (615, 750, and 1486.6 eV), as shown by the solid black circles in the main frame of Figure 4. The spectra show several features that exhibit systematic changes with the photon energy. At the lowest photon energy, $h\nu = 615$ eV, the spectrum is dominated by a peak at 162.5 eV with a shoulder at 163.6 eV. These spectral features, which are separated by 1.1 eV, are readily assigned to the spin−orbit doublet feature of S $2p_{3/2}$ at 162.5 eV and S $2p_{1/2}$ at 163.6 eV. There are also two additional weaker features at ∼161 and 166.8 eV. The intensities of these two features increase with increasing photon energy, suggesting a common origin such as a spin−orbit split doublet. From the binding energy and the spin−orbit splitting, it is evident that these features are due to the Se 3p core levels, with the peaks at 161 and 166.8 eV assigned to Se $3p_{3/2}$ and Se $3p_{1/2}$, respectively, with a spin−orbit splitting of 5.8 eV. While it is easy to identify signals due to

(30) Maiti, K.; Kumar, A.; Sarma, D. D.; Weschke, E.; Kaindl, G. *Phys. Rev. B* **2004**, *70*, 195112.
(31) Maiti, K.; Manju, U.; Ray, S.; Mahadevan, P.; Inoue, I. H.; Carbone, C.; Sarma, D. D. *Phys. Rev. B* **2006**, *73*, 052508.
(32) Nagarkar, P. V.; Kulkarni, S. K.; Umbach, E. *Appl. Surf. Sci.* **1987**, *29*, 194.
(33) Kulkarni, S. K.; Winkler, U.; Deshmukh, N.; Borse, P. H.; Fink, R.; Umbach, E. *Appl. Surf. Sci.* **2001**, *169−170*, 438.
(34) Borchert, H.; Haubold, S.; Haase, M.; Weller, H.; McGinley, C.; Riedler, M.; Möller, T. *Nano Lett.* **2002**, *2*, 151.
(35) Borchert, H.; Talapin, D. V.; McGinley, C.; Adam, S.; Lobo, A.; de Castro, A. R. B.; Möller, T.; Weller, H. *J. Chem. Phys.* **2003**, *119*, 1800.
(36) Tanuma, S.; Powell, C. J.; Penn, D. R. *Surf. Interface Anal.* **1988**, *11*, 577.
(37) Tanuma, S.; Powell, C. J.; Penn, D. R. *Surf. Interface Anal.* **1991**, *17*, 927.

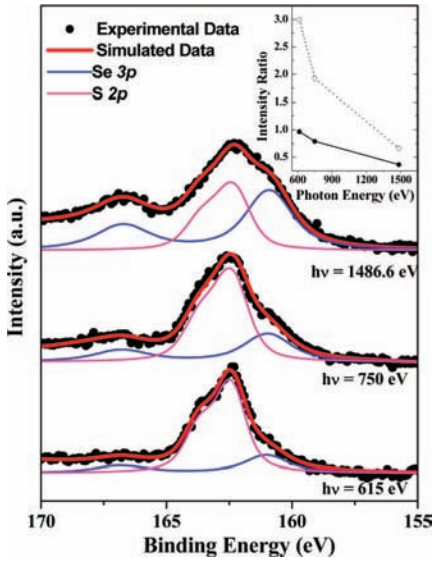

Figure 4. High-resolution photon emission spectra of the S 2p and Se 3p core levels at various energies. At each energy, the experimental data are shown by the solid black circles and the total fit by the thick red line, which is the sum of two independent component functions, S 2p (magenta) and Se 3p (blue). The inset shows the S 2p/Se 3p intensity ratios obtained with (○) and without (●) consideration of the photoemission cross section (the lines are guides to the eye).

one S species (at 162.5 and 163.6 eV) and one Se species (at 161.0 and 168.8 eV), it is in general possible to have multiple species of these elements in a nanocluster, as has been discussed in the literature.[21,22,28] In order to determine the number of S and Se species contributing to the signal in Figure 4, we carried out detailed spectral decompositions for differing numbers of S and Se species. It was found that all of these spectra could be consistently described with a single species of S and Se, whereas use of more than one species of S and Se most often led to physically meaningless parameters, such as negative intensities. We show in Figure 4 the results of the decomposition of the experimental data (solid circles) for S01 at each energy in terms of the S and Se components (the thin solid lines) along with their sum (the thick solid line, termed "Simulated Data"), which overlaps the experimental data in Figure 4, showing a very good agreement in every case. We note that such analyses were also carried out for the other two samples (shown in Figure S7 in the Supporting Information) and yielded very similar conclusions.

Evidently, the relative intensity of the Se 3p signals increases rapidly with increasing photon energy. We have plotted in the inset of Figure 4 the relative S 2p/Se 3p intensity ratio as a function of the photon energy, marked by the solid circles. The rapid increase may arise from a higher abundance of Se away from the surface region or near the core region as well as from a change in the photoemission cross section of Se 3p relative to that of S 2p as a function of photon energy. In order to distinguish between these two effects, we have normalized the relative intensities of Se 3p and S 2p with the corresponding photoemission cross section[38] and shown it as the open circles in the same inset. Clearly, there is a significant increase in the Se 3p relative intensity with the photon energy beyond the change in the photoemission cross section, thereby signaling a strongly heterogeneous distribution of the elements in these samples.

(38) Yeh, J. J.; Lindau, I. *At. Data Nucl. Data Tables* **1985**, *32*, 1.

In order to go beyond the above-mentioned qualitative statement of heterogeneity of the composition, we carried out a detailed quantitative analysis of the relative intensities. The methodology is essentially similar to that used in an earlier paper,[21] though it was then applied only to a homogeneous core-only structure. In this method, the intensity contribution dI to any core level from a volume element dv of the sample at a depth d from the surface is given by

$$\mathrm{d}I = n\sigma I_0 \exp\left(-\frac{d}{\lambda}\right)\mathrm{d}v \tag{1}$$

where λ is the mean free path, σ is the photoemission cross section, I_0 is the instrumental factor, which depends on the photon flux, the experimental geometry, and the transmission coefficient of the analyzer at that particular energy, and n is the number density of the particular element in whose core level we are interested. In a homogeneous system, n is characterized by a single number; however, in the presence of heterogeneity of any kind, n is in general a function of d [i.e., $n = n(d)$]. Therefore, it is this crucial appearance of $n(d)$ in the above equation that allows us to delineate between different models, identifying the specific $n(d)$ functions for S and Se that are compatible with the intensity variations observed. It should also be noted that I_0 is in general very difficult to estimate reliably. Instead, we consider the ratios of S and Se intensities throughout our analysis, since the transmission efficiency is the same for both because these two core-level signals appear at almost the same energy. Similarly, geometrical factors as well as the photon flux are necessarily identical for the two core levels, as their spectra are simultaneously collected in the same experiment. Thus, the intensity ratio removes I_0 from our analysis altogether. The intensity ratio, $I^{\mathrm{Se}}/I^{\mathrm{S}}$, is given[21] by

$$\frac{I^{\mathrm{Se}}}{I^{\mathrm{S}}} = \frac{\int \mathrm{d}I^{\mathrm{Se}}}{\int \mathrm{d}I^{\mathrm{S}}} = \frac{\sigma^{\mathrm{Se}}}{\sigma^{\mathrm{S}}} \frac{\int_{R'}^{R''}\int_0^{\pi}\int_0^{2\pi} n^{\mathrm{Se}}(r)\exp\left(-\frac{f(r,\theta)}{\lambda}\right)r^2\sin\theta\,\mathrm{d}\theta\,\mathrm{d}\varphi}{\int_{R'}^{R''}\int_0^{\pi}\int_0^{2\pi} n^{\mathrm{S}}(r)\exp\left(-\frac{f(r,\theta)}{\lambda}\right)r^2\sin\theta\,\mathrm{d}\theta\,\mathrm{d}\varphi} \tag{2}$$

In the above expression, we have used the spherical symmetry of the nanoparticles suggested by TEM images (Figure 2 and Figure S4 in the Supporting Information) to express the relation in spherical polar coordinates. Furthermore, we have assumed that the compositional variation is also spherically symmetric, keeping in mind the intermediates generated in the synthetic process. These assumptions allow us to replace $n(d)$ with a function $n(r)$ that has no dependence on θ and φ. The quantity $f(r, \theta) = (R^2 - r^2 \sin^2 \theta)^{1/2} - r \cos \theta$ is a function[21] that measures the distance d of a point (r, θ, φ) from the surface of the sphere, the spherical symmetry ensuring that d is independent of φ when the z axis is chosen to lie along the direction of the photoelectron emission.

As we have already pointed out, $n(r)$ contains the model-specific information. For example, $n^{\mathrm{Se}}(r)$ and $n^{\mathrm{S}}(r)$, which represent the number densities of Se and S, are given by

$$\begin{aligned} n^{\mathrm{Se}}(r) &= 1 \qquad r_1 < r \le r_2 \\ &= 0 \qquad \text{elsewhere} \end{aligned}$$

$$\begin{aligned} n^{\mathrm{S}}(r) &= 1 \qquad 0 < r \le r_1 \text{ and } r_2 < r \le r_3 \\ &= 0 \qquad \text{elsewhere} \end{aligned}$$

for the model shown in Figure 3a. In order to extract the functions $n^{\mathrm{Se}}(r)$ and $n^{\mathrm{S}}(r)$ that are most compatible with

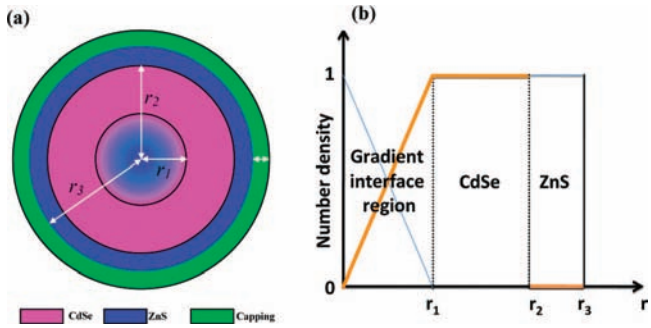

Figure 5. (a) Schematic model of the heterostructured nanomaterial, which has three main layers: a gradient inhomogeneous alloy in the core ($0 < r \leq r_1$) followed by a thick shell of CdSe ($r_1 < r \leq r_2$) and a thinner shell of ZnS ($r_2 < r \leq r_3$). (b) Schematic representation of the variation of the chemical composition for the final model.

experimentally observed variation of the relative intensity I^{Se}/I^{S} with photon energy, we considered various models, including the three shown in Figure 3, thereby defining both $n(r)$ as a function of various radii (i.e., r_1, r_2, r_3, etc.). Since I^{Se}/I^{S} in eq 2 depends on the specific choices for all of these radii, we can obtain the values of these radii by requiring the best description of the intensity ratios as a function of the photon energy via a least-squared-error minimization procedure, which yields for each model a set of optimal values for these radii. We note that an unconstrained error minimization process such as that described above invariably leads us to some results without any reference to the reliability of the derived model to describe the real system.[24] It is hence difficult, if not impossible, to use photoemission data such as those given above to derive a description for such complex heterostructures. However, we found that it is possible to discriminate the unrealistic solutions from the meaningful ones by constraining the model to be consistent with two additional quantities, namely, the total size of the nanocrystals and the overall composition. These two quantities are readily and accurately determined from TEM and ICP−AES, respectively, for any system. With these additional constraints, we found that none of the three models shown in Figure 3 are consistent with the observed photoemission experiments with different photon energies. The only model that was found to be consistent with all of the experimental results, namely the ones from photoemission, TEM, and ICP−AES, is shown in Figure 5. This model has a graded core region in which the pure ZnS at the core continuously changes in composition to smoothly become CdSe at a radius r_1; this core region is followed by a shell of pure CdSe up to a radius r_2, which is in turn finally capped by a layer of ZnS up to radius r_3.

In hindsight, this model appears to be a reasonable one in view of the known stabilities of the parent binary phases and the synthetic conditions used. As already described, the synthesis of these samples involves the addition of $[Et_3NH]_4[Cd_{10}Se_4(SPh)_{16}]$ in a reaction medium containing the dispersion of preformed ZnS nanocrystals. Since cadmium sulfides and selenides are much more stable than those of zinc, ZnS nanoparticles are expected to undergo ion exchange with those in the reaction mixture, forming an alloyed core system. Indeed, we have established that Cd(II) can indeed undergo ion exchange with Zn(II) of the ZnS core (details are provided in Figure S8 and the associated text in the Supporting Information). It is reasonable to suggest that the alloy formed in the core is not homogeneous, with the center of the core being closer to pure ZnS and the surface closer to CdSe, as the ion exchange with the interior of the core region becomes increasingly more difficult. To establish that the formation of this graded core was not aided by the presence of any unreacted Zn/S precursor on the bare ZnS nanoparticles, which may then react with the Cd/Se precursor to form a graded structure, we carried out XPS experiments on the bare ZnS nanoparticles (results shown in Figure S9 in the Supporting Information) and found only one species each of Zn and S present in the cluster. This observation suggests that there is no unreacted Zn/S precursor on the surface of the ZnS nanoparticles and hence that the graded alloy formation is indeed due to the interaction of the Cd/Se precursor with the ZnS core. This graded structure also helps the growth of the eventual layer of CdSe on the top of the core region, as the graded alloy composition offers an ideal way to achieve smooth lattice matching between the core region and the overlayer. Once the layer of CdSe is grown, the second step of the synthesis process, the composite graded core−CdSe shell particles are placed in a reaction mixture with zinc and sulfur ions in order to grow the final layer of ZnS in the intended QDQW structure. It is interesting to note that our results are consistent with a sharp interface between the CdSe layer and the outermost ZnS layer, unlike the ZnS graded core−CdSe overlayer region. This observation of a sharp interface between the outermost layers is consistent with the relative reactivities discussed earlier: the Zn/S precursor in the reaction mixture is unable to displace ions from the more stable CdSe layer. To check whether this sharp CdSe/ZnS interface is a result of the heating being restricted to 180 °C, we performed a control experiment in which sample S02 was heated at 210 °C for 30 min. The synthesis and characterization of the sample after heating, designated as S02B, has been discussed in some detail in Figures S10−S13 and the associated text in the Supporting Information. We carried out a comparative photoemission experiment on the original sample (S02) and the sample after heating (S02B). We found that the Cd 3d/Zn $2p_{3/2}$ ratios before and after the heating were 3.10 and 2.71, respectively, as indicated by the decrease in the normalized Cd spectral intensity after heating (see Figure S14 in the Supporting Information). When the exponentially dependent surface sensitivity of XPS is taken into account, as discussed earlier, it is clear that there is no migration of Cd ions toward the outermost ZnS layer even upon heating to 210 °C, thereby suggesting that the sharp outer interface is not a consequence of heating at the lower (180 °C) temperature.

We assume that the composition variation along the radial direction is linear, with pure ZnS at the center and pure CdSe on the surface of the graded core region. This precept is of course an assumption, and the real situation may be somewhat more complex. However, though it is straightforward to include such dependencies within our model, doing so would increase the number of parameters in the fitting procedure. In view of this fact, and also because such complications in the model introduce only minor quantitative changes and no qualitative change, we have analyzed all of our results in terms of a linear dependence. The error minimization leads to the result that the characteristic radii r_1, r_2, and r_3 defined in Figure 5 have the optimal values shown in Table 1 for the three samples analyzed. Samples S02 and S03 exhibit gradient core radii (r_1) of 1.15 and 1.25 nm, respectively, while sample S01 has a somewhat bigger gradient core radius (1.93 nm), possibly as a result of the use of larger amount of Cd/Se precursor in this case. It is to be noted here that the gradient core radii (r_1) for all of the samples are a little bit bigger than the radius of the bare ZnS nanoparticles (~1.1 nm) because of the incorporation of additional atoms in the ZnS core leading to the graded core

Table 2. Band Gaps (eV) Calculated by the Tight Binding Method for Three-Shell QDQW Structures with the Radii of the Three Shells As Shown in Table 1 and either a Pure ZnS Core (Figure 3a) or a Graded Core Region (Figure 5); Experimental Band Gaps Measured Using UV Absorption Spectroscopy Are Also Given

sample number	ZnS core	gradient core	exptl
S01	2.10	2.02	2.00
S02	2.26	2.18	2.10
S03	2.55	2.25	2.23

region. In the same table, we have also included the Cd/Zn elemental ratio calculated on the basis of the model along with the optimized parameter values; the corresponding values from ICP−AES as well as the total sizes of the particles obtained from TEM are given in parentheses for easy comparison. Clearly, in every case there is a good correspondence between the model parameters derived from the simulation of the photoemission intensity variation with photon energy and those obtained from the independent experimental ICP−AES and TEM measurements. This work shows that the efficient use of these experimental values can very effectively distinguish between different models, helping one to identify the physically meaningful solution from several other solutions possible from the simulation of photoemission signal intensities alone.

To provide an independent verification of our results, we calculated the band gaps of all three structures mentioned in Table 1 using an accurate tight binding (TB) model reported previously.[39−41] The electronic structures of the actual atomic arrangements corresponding to different models were calculated with the optimized radii (Table 1) for each of the samples, the diagonal and off-diagonal terms of the TB Hamiltonian being parametrized to provide an accurate description of the electronic structure of the bulk systems. Using these previously estimated parameter values,[39−41] we calculated the energy-level diagram for the states corresponding to each of the samples. The band gaps were directly obtained as the difference between the two relevant energy levels, namely, the highest occupied molecular orbital (HOMO) and lowest unoccupied molecular orbital (LUMO) corresponding to the eigenstates of the cluster. For each sample, we considered two cases. In the first case, we considered a QDQW with a pure ZnS core of radius r_1 without any intermixing. The second case, in contrast, consisted of a graded alloy core of ZnS and CdSe to radius r_1, as suggested by our analysis. The resulting band gaps for these two models of the internal structure are given in Table 2 along with the band gaps measured experimentally from the peaks of the absorption spectra. The results make it evident that the introduction of the graded core reduces the band gap compared with that in the case of a pure ZnS core. More importantly, we find that for all three samples, the band gap calculated assuming a graded core provides the best agreement with that measured from the absorption spectra.

(39) Sapra, S.; Shanti, N.; Sarma, D. D. *Phys. Rev. B* **2002**, *66*, 205202.
(40) Sapra, S.; Sarma, D. D. *Phys. Rev. B* **2004**, *69*, 125304.
(41) Viswanatha, R.; Sapra, S.; Saha-Dasgupta, T.; Sarma, D. D. *Phys. Rev. B* **2005**, *72*, 045333.

4. Conclusion

In conclusion, we have shown that X-ray photoelectron spectroscopy can provide layer-resolved information on the internal structure of highly complex heterostructured nanocrystals because of the technique's extremely short depth of probing that matches the dimensions of such nanocrystals. This short depth, characterized by the inelastic mean free path of photoejected electrons, can be varied by changing the photon energy over the wide range available from a high-brilliance synchrotron source, thereby making quantitative analysis possible. However, such analysis does not always lead to a unique description of highly complex nanocrystals. We have shown that this problem can be overcome by requiring that the description of the internal structure obtained from photoelectron spectroscopy analysis be consistent with two independent measurements, namely, the overall composition ratio and the total size (diameter) of the nanocrystals as obtained from ICP−AES and TEM, respectively, leading to accurate descriptions of such nanocrystal systems. These analyses show that attempted overlayer growth on preformed nanoclusters of a different material does not necessarily lead to a sharp interface and that the nature of the composite depends on the details of the reactivities of different components. Specifically, in the present case, growth of a CdSe layer on top of ZnS nanocrystals leads to the formation of a graded ZnS/CdSe alloy in the core region as a result of extensive ion exchange between the solid and the reactants; interestingly, however, treating this composite system with a reaction mixture containing Zn/S precursor leads to the formation of a capping layer of ZnS with a sharp interface and minimal intermixing. These distinctive behaviors in the two steps attempting to grow overlayers on top of a core nanocrystal can be easily understood in terms of differences in stability. Finally, by calculating the band gaps for different models of the internal structure, we have shown that it would be impossible to account for the optical properties of such nanomaterials without taking into account the details of such interesting and subtle composition variations in complex, heterogeneous nanocrystals materials.

Acknowledgment. This work was supported by the Department of Science and Technology, Government of India. The authors acknowledge the financial support of the International Centre for Theoretical Physics (ICTP) under the ICTP−ELETTRA Users Program and the Indo−Italian Bilateral Exchange Program for synchrotron radiation experiments at ELETTRA. D.D.S. acknowledges the J. C. Bose National Fellowship. The work was also supported by the University of Manchester and the EPSRC.

Supporting Information Available: UV−vis, PL, and core-level XPS spectra for bare ZnS nanoparticles; UV−vis and PL spectra and TEM images for the ZnS/CdSe particles and two other QDQW systems along with their decomposed XPS spectra; high surface sensitivity of the photon energy illustrated using Cd 3d and N 1s core-level spectra; UV−vis absorption spectra at various times after addition of cadmium acetate to preformed ZnS nanoparticles at a higher temperature; and details of the synthesis and characterization of sample S02B. This material is available free of charge via the Internet at http://pubs.acs.org.

JA8033075